Miscibility Gap Closure, Interface Morphology, and Phase Microstructure of 3D Li_xFePO_4 Nanoparticles from Surface Wetting and Coherency Strain

Michael J. Welland,*,† Dmitry Karpeyev,‡ Devin T. O'Connor,§,∥ and Olle Heinonen†,‡,⊥

†Materials Science Division, Argonne National Laboratory, Argonne, Illinois 60439, United States, ‡Computation Institute, University of Chicago, Chicago, Illinois 60637, United States, §McCormick School of Engineering, Northwestern University, Evanston, Illinois 60208, United States, and ⊥Northwestern-Argonne Institute for Science and Engineering, Evanston, Illinois 60208, United States. ∥Present address: National Institute of Standards and Technology, Boulder, CO, United States.

ABSTRACT We study the mesoscopic effects which modify phase-segregation in Li_xFePO_4 nanoparticles using a multiphysics phase-field model implement on a high performance cluster. We simulate 3D spherical particles of radii from 3 to 40 nm and examine the equilibrium microstructure and voltage profiles as they depend on size and overall lithiation. The model includes anisotropic, concentration-dependent elastic moduli, misfit strain, and facet dependent surface wetting within a Cahn–Hilliard formulation. We find that the miscibility gap vanishes for particles of radius ∼5 nm, and the solubility limits change with overall particle lithiation. Surface wetting stabilizes minority phases by aligning them with energetically beneficial facets. The equilibrium voltage profile is modified by these effects in magnitude, and the length and slope of the voltage plateau during two-phase coexistence.

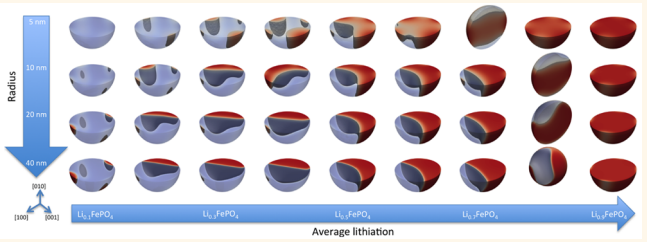

KEYWORDS: Li-ion battery · $LiFePO_4$ · phase-field model · coherency strain · interface morphology · surface wetting · nanoparticles

A great deal of interest has been generated for $LiFePO_4$ as an inexpensive and environmentally friendly electrode material for future generations of Li-ion batteries.[1−4] Bulk systems, *i.e.*, systems with a small surface to volume ratio such that surface effects can be ignored, of varying degrees of overall lithiation are known to separate almost completely into regions of $LiFePO_4$ and $FePO_4$. Such bulk systems exhibit slow (dis)charge rates due to poor electronic and ionic conductivities in both $LiFePO_4$ and $FePO_4$, while the diffuse interfacial region spanning intermediate concentrations of Li_xFePO_4 is considered efficient in the intercalation reaction.[5−8] It was found experimentally that nanoparticles at room temperature exhibit remarkably high (dis)charge rates and are therefore of interest for high power density materials.[9,10] A theory for the remarkable increase in (dis)charge rate is that nanosizing suppresses phase-segregation that occurs in bulk systems, and leads to a single phase Li_xFePO_4 solution in nanoparticles over the range of concentrations which exhibit the efficient reaction mechanism.[2,3,11] Experiments on Li_xFePO_4 consistently show that there does appear to be a size dependent miscibility gap which disappears at small particle sizes, although the precise mechanism for the stabilization of the homogeneous solid solution phase at intermediate concentrations of Li_xFePO_4 remains unclear despite numerous experimental and theoretical investigations.[5,9,12]

The phase diagram of bulk-Li_xFePO_4 shows a large miscibility gap at room temperature bounded by narrow solid solution of $Li_{0.032}FePO_4$ and $Li_{0.962}FePO_4$.[6,7] The disappearance of the miscibility gap and shifting in the solubility limits is observable both by the disappearance of the cell voltage plateau and by direct observation of structure and composition.[9,10,12,13] The voltage can be measured *in situ*, but such measurements are typically done on an ensemble of particles of a particular size distribution and therefore does not indicate if particles of different sizes lithiate concurrently with a

* Address correspondence to mike@mikewelland.com.

Received for review April 28, 2015 and accepted September 10, 2015.

Published online September 10, 2015
10.1021/acsnano.5b02555

diminished miscibility gap, or sequentially based on a size-dependent nucleation mechanism.[3,14] Observation of the local crystal structure and composition by X-ray, neutron diffraction, and TEM indicates a reduction in the miscibility gap as a function of particle size, and a shift in the solubility limits depending on the overall particle concentration.[10,12,15,16] Complete disappearance of the miscibility gap has been proposed at particle diameter of 15 nm at room temperature.[9]

The reduction of the miscibility gap with particle size has many possible explanations. It could be accounted for by confinement of the diffuse interface, which is observed to be approximately 4 nm wide, by the particle geometry.[12,15,17,18] Coherency strain between phases may also play a role as the orthorhombic (space group *Pnma*) lattice expands by as much as 5% in [100] and [010] but contracts by ~1.9% in [001] upon lithiation.[19,20] The superior ability of nanoparticles to accommodate strain through surface relaxation, and the large volume of the interface relative to the particle may then stabilize intermediate concentrations elastically.[9] Finally, surface energy and wetting can also play a more direct role in the alteration of the phase diagram.[21]

Elasticity may also contribute to the microstructures observed experimentally in both plate-like and spherical particles. Chen *et al.* performed TEM analysis on chemically delithiated, platelike particles of approximate dimensions $4 \times 2 \times 0.2\,\mu m^3$ with large, diamond-like {010} faces with the long axis along [001].[17] They noted alternating stripes of $LiFePO_4$ and $FePO_4$ approximately 100 nm wide and oriented along (100) with dislocation features aligned in similar planes.[17] Ramana *et al.* later performed similar experiments with more spherical, but still faceted, particles with large {010} faces and long axes parallel to [001], of diameter ~100 nm.[15] They also observed the (100) interface, and in addition interfaces parallel to [101] and [100], noting that the latter two interfaces appear to be sharper than the (100).[15] The interface orientation may result from anisotropy in the elastic constants and misfit strains.[14,22] Cogswell and Bazant predicted the elastic strain energy of interfaces as a function of orientation, assuming the same elastic modulus in each phase, and concluded that the {101} planes were optimal for coherent interfaces and that {100} interfaces may arise from loss of coherency.[14,23]

Complex surface behavior that depends on crystallographic facets has been observed, including preferential (de)lithitation and a modified surface layer described as a disordered but not amorphous layer of approximately 3 nm thickness.[16,18,24−28] Carbon coating of the particles, which is frequently done to improve conductivity, appears to reduce the amount of disorder in this surface layer and mitigate the reduction of the miscibility gap.[28,29] Raman scattering revealed that the surface of intermediate average concentrations is biphasic, which is contradictory to early core−shell models.[8,15,26] Chen *et al.* observed that, upon cooling from a homogeneous solution, $LiFePO_4$ formed at the large {010} surfaces, while Boesenberg and Lucas observed accumulation of $FePO_4$ on the other surfaces perpendicular to (010).[24,25,30] Wang *et al.* performed first principle studies of the surface energies of $LiFePO_4$ and reported significantly different energies between $LiFePO_4$ and $FePO_4$, depending on the facet which, as Cogswell *et al.* described, can lead to a solid state phenomenon akin to fluid surface wetting.[31,32]

Previous phase-field models have been applied to simulate nanoscale Li_xFePO_4 particles with various simplifications to elasticity and surface wetting, and are furthermore limited to 1D or 2D.[11,14,32,33] Burch and Bazant modeled the effect of confinement of the diffuse interface by particle size using a 1D phase-field model without coherency strain.[18] Wagemaker *et al.* later performed similar simulations and compared them to experiments, which showed a size-dependent miscibility gap accompanying solubility limits that depend on average particle concentration.[12] Zeng and Bazant used a 1D spherically symmetric model to study high rates but spherical symmetry is experimentally known to not be correct in common applications.[34] 2D models in the (001) plane were developed by Dargaville *et al.* but simplify the effects of anisotropic coherency strain and neglect surface wetting.[35] Other models reduce the geometry to 2D with a "depth-averaged" approximation along [010] assuming thin plate-like particles, fast diffusion along [010] channels, and an intercalation reaction on the out-of-plane (010) surface. These models predicted intercalation waves,[33] and bypassing of decomposition kinetically.[11] Cogswell and Bazant incorporated coherency strain into their model with constant elastic constants between phases and showed the appearance of alternating stripe patterns with {101} interfaces in agreement observed microstructures. However, in their work, the local displacement was fixed at the boundaries. While they allowed for a macroscopic homogeneous strains to relax the overall stress, this procedure does not correspond to a free surface with zero traction.[14,24] Later, Cogswell and Bazant incorporated facet-dependent surface wetting into a 2D depth averaged model and also proposed that coherency strain would form an elastic energy-governed nucleation barrier.[32] However, they simplified facet-dependent wetting to a Dirichlet boundary condition, which is justifiable in the thin interface approximation[14] but which may not be true in the general case where volumetric forces may overwhelm those on the surface.[32]

In the current work, we develop a comprehensive phase-field model in 3D, solved numerically on a high performance computer cluster. We simulate the equilibrium interface morphology and orientation considering elasticity with concentration-dependent lattice

constants and elastic moduli and free surfaces. Spinodal decomposition is included within a Cahn–Hilliard phase-field model that incorporates surface wetting as a natural boundary condition. This implementation of surface wetting allows for the possibility that volumetric thermodynamic forces may overcome those on the surface. We perform parameter sweeps for average particle concentrations between $Li_{0.05}FePO_4$ and $Li_{0.95}FePO_4$ and for particle radii of 3, 5, 10, 20, and 40 nm. The simulated equilibrium states of particles of different size and average lithium concentration are investigated systematically in order to separate the equilibrium thermodynamics from questions of lithiation kinetics and pathways. This work features spherical particles (as may result from ball milling), but due to implementation in a Finite Element framework, it is applicable to other geometries too. Simulation results show the closure of the miscibility gap, shifting of solubility limits, and modified interface morphology as a consequence of the chemical, elastic, and surface forces. Surface wetting is shown to stabilize minority phases through aligning them with energetically beneficial facets. This is an important conclusion, as modification of surface wetting through, *i.e.*, coatings, may present an opportunity for future electrode material optimization.

MODEL DEVELOPMENT

We consider the system to be hosted in a matrix of $FePO_4$ of density ρ. The solid solution Li_xFePO_4 is modeled as a solution between occupied and vacant Li sites with local concentration $c_{Li} = \rho x$ and $c_{vacancy} = \rho[1 - x]$. Thus, x is defined as in Li_xFePO_4, the local fraction of occupied Li sites. The Helmholtz energy functional of the system is written integrating over the volume, V, and surface, S:

$$F = \int_V \left\{ f + \frac{1}{2}\boldsymbol{\sigma} : \epsilon_{el} + \frac{\kappa}{2}|\nabla x|^2 \right\} dV + \int_S \left\{ f^s[1 + \mathrm{tr}(\epsilon^s)] + \frac{1}{2}\boldsymbol{\sigma^s} : \epsilon^s_{el} \right\} dS \quad (1)$$

where f is the chemical free energy density, $\boldsymbol{\sigma}$ and ϵ_{el} are the stress and infinitesimal elastic strain tensors, respectively, and κ is the isotropic coefficient of the gradient energy term in the Cahn–Hilliard model. The corresponding surface quantities are denoted by superscript S, *e.g.*, f^S. Although we are considering a small strain approximation, we scale the surface energy by the surface dilation, $1 + \mathrm{tr}(\epsilon^s)$, where ϵ^s is the total surface strain, in order to capture surface area minimization. We consider the surface stress to be calculated in the undeformed domain and is therefore not scaled.

The chemical surface free energy density, f^S is calculated

$$f^s = \gamma_{FePO_4} + x\Delta\gamma + f^{s,0} \quad (2)$$

where γ_{FePO_4} is the facet dependent surface energy of $FePO_4$, and $\Delta\gamma = \gamma_{LiFePO_4} - \gamma_{FePO_4}$ is the surface energy difference between $LiFePO_4$ and $FePO_4$. It was found numerically that a simple linear function caused numerical problems since it does not have a minimum. Therefore, an extra term $f^{s,0} = 0.2/x[1 - x]$ was added to f^S that asymptotically approaches infinity as $x \to 0,1$, the magnitude of which was fit to provide minima at approximately $x = 0.03, 0.97$.

The local volumetric stress is $\boldsymbol{\sigma} = \boldsymbol{C}:\epsilon_{el}$, where $\boldsymbol{C}$ is the rank-4 orthorhombic stiffness tensor. The stiffness tensor is assumed to be a linear interpolation between $\boldsymbol{C}_{FePO4}$ and $\boldsymbol{C}_{LiFePO4}$, the moduli for $LiFePO_4$ and $FePO_4$, respectively:

$$\boldsymbol{C} = [1 - x]\boldsymbol{C}_{FePO4} + x\boldsymbol{C}_{LiFePO4} \quad (3)$$

The elastic strain is calculated from the total strain minus the misfit strain $\Delta\epsilon$, which is assumed to be a linear interpolation between the lithiated and delithiated lattice constants according to Vergard's law:

$$\epsilon_{el} = \epsilon - x\Delta\epsilon \quad (4)$$

The total strain is calculated from the displacement field, $\vec{u}$ by

$$\epsilon = \frac{1}{2}[\nabla\vec{u} + (\nabla\vec{u})^T]$$

The surface stress is $\boldsymbol{\sigma^s} = \boldsymbol{C^s}:\epsilon^s_{el}$ where $\boldsymbol{C^s}$ is the surface stiffness tensor and is assumed to be independent of concentration. The surface strain ϵ^s_{el} is calculated by projecting the strain onto the surface tangent plane using the operator $\boldsymbol{P} = \mathbf{1} - \hat{n}\otimes\hat{n}$, where $\hat{n}$ is the outward unit normal vector to the surface,[36] and $\mathbf{1}$ is the rank-2 identity tensor.

Although the density varies by 5.7% between the lithiated and delithiated phases, ρ is held constant to the density of the delithiated phase, 23 273 mol m^{-3}.[20] This approximation is necessary since the simulated geometry does not change volume with phase and therefore varying density would imply a lack of mass conservation. The chemical potential of Li is thus related to the occupancy fraction by

$$\mu = \frac{\delta F}{\delta c_{Li}} = \frac{1}{\rho}\frac{\delta F}{\delta x}$$

Using eq 1, the variations in the bulk and on the boundary are over a space of smooth functions so both terms multiplying the bulk and boundary variation δc must vanish independently:[37,38]

$$\mu = \frac{1}{\rho}\left[\frac{\partial\left(f + \frac{1}{2}\boldsymbol{\sigma} : \epsilon_{el}\right)}{\partial x} - \kappa\nabla^2 x\right] \text{ on } V \quad (5)$$

$$0 = \frac{1}{\rho}[\Delta\gamma[1 + \mathrm{tr}(\epsilon^s)] + \hat{n}\cdot\kappa\nabla x] \text{ on } S$$

where surface wetting is incorporated as a natural boundary condition.[14,34,39] The effect of $\Delta\gamma$ is thus

incorporated as a natural boundary condition for the chemical potential. The flux of Li, $\vec{J}$, is

$$\vec{J} = -\rho \frac{x[1-x]}{RT} \boldsymbol{D} \cdot \nabla \mu \quad (6)$$

where $\boldsymbol{D}$ is the anisotropic diffusion tensor. We will model the time evolution of the system using standard phase field equations obtained from Onsager nonequilibrium thermodynamics. Finally, mass conservation is expressed as

$$\rho \frac{dx}{dt} = -\nabla \cdot \vec{J} \quad (7)$$

To avoid fourth order spatial derivatives in solving the Cahn−Hilliard problem, the fourth-order diffusion problem above is split into a mixed formulation where μ is solved as a second-order equation according to eq 5 and x is solved as a second-order PDE according to eq 7 with zero flux boundary conditions. As described in the Methods section, a transformation on the x variable is performed to ensure $0 > x > 1$ so as to avoid difficulties associated with the logarithms in eq 1 during the numerical solving process.

Due to the fast rate of elastic relaxation in solids, elastomechanics is solved quasistatically using a virtual work formulation

$$0 = \int_V \{\boldsymbol{\sigma} : \delta\epsilon\}\, dV + \int_S \{f^s \mathrm{tr}(\delta\epsilon^s) + \boldsymbol{\sigma}^s : \delta\epsilon^s\}\, dS \quad (8)$$

where $\delta\epsilon$ represents a virtual variation in the strain field, which is projected onto the surface *via* the projection operator defined above.

Surface Energy. First principle calculations of surface energies for facets of $LiFePO_4$ and $FePO_4$ show strong dependence on the state of lithiation in addition to facet orientation.[31] Surface energy therefore produces both a constrictive force around the surface, as well as surface *wetting* in the solid state as discussed by Cogswell *et al.*[32] Surface wetting leads to the (de)lithiation of particular surfaces depending on their orientation, an effect which has been noticed experimentally.[24,25,30]

Surface wetting is implemented in the current work *via* eq 5.[39] In this form, while the boundary condition is generally sufficient to keep the facet (de)lithiated, the volumetric thermodynamic forces, such as interface continuity and elasticity, may dominate over the surface wetting effect with the consequence that facets that would be de(lithiated) as per surface energy reduction, may not be.

To consider arbitrary surface orientation, we interpolate γ_{FePO_4} and $\Delta\gamma$ from Wang *et al.*[31] into spherical coordinates. We define θ as the polar angle from the [010] direction and ϕ as the azimuthal angle from the [100] direction about [010]. To obtain reasonable polynomial interpolations, an additional (001) surface with properties identical to (201) was added. The resulting interpolations for are shown in Figure 1. To minimize the energy at the surface, Li will wet surfaces for negative values $\Delta\gamma$ and dewet positive values. The color maps of these figures have been reversed so that the colors here match the colormap of x used later.

RESULTS

Simulations are preformed for average particle concentrations, denoted by $\bar{x}$, of 0.05, 0.1, 0.2, 0.3, 0.4, 0.5, 0.6, 0.7, 0.8, 0.9, 0.95 for a range of radii from 3 to 40 nm. (The validity of a continuum treatment of particles on the order of 3 nm is questionable, but is performed here as a lower limit of the current study.) All figures are deformed according to the calculated displacement field $\vec{u}$, with no scaling factor. In presenting 3D results, $x < 0.5$ is made translucent in order to show the internal contours of the microstructure. Simulation results are typically symmetric, often about the (010) surface that includes the origin. Where symmetry was observed, one of the hemispheres has been removed to aid in visualization.

Simulations calculate the spatial distributions of variables x, μ, and $\vec{u}$ at each time step, from which only the final time step is relevant in the current discussion. In equilibrium, the chemical potential μ is constant everywhere and is converted into the corresponding cell voltage by the equation:

$$V = -\frac{\mu_{Li}}{e} + V^0 \quad (9)$$

where e is the elementary positive charge and V^0 is the reference voltage.[3,40] In bulk thermodynamics, the case of a transition between two stable phases should occur at a constant μ_{Li}, resulting in a constant voltage over the range of two-phase coexistence.

Data reduction of the simulated Li concentration field is important in order to concisely summarize the results across a number of particles and reveal trends. In bulk equilibrium systems, the spatially varying x field consists of large regions of $x = 0.03$ and 0.97, corresponding to $FePO_4$ and $LiFePO_4$ phases, respectively, separated by an interface of relatively negligible width. These two compositions are concisely recorded on the phase diagram as phase boundaries. For the smaller particles in our study, the x field is no longer cleanly divided to the solubility limits due to relatively significant interface width and thermodynamic forces that are influenced by particle size. Rather, the field assumes a more distributed range of values over the volume of the particle. To reduce these simulation results systematically and present them in a useful manner on a *nano*- phase diagram, the following procedure is followed. We calculate an approximate probability density function [PDF] by integrating a Gaussian with variance $\sigma = 0.01$ over the volume:

$$\mathrm{PDF}(x') = \frac{1}{\sigma\sqrt{2\pi}} \int_V e^{-[1/2][(x-x')/0.01]^2}\, dV \quad (10)$$

and similarly for the surface. Local maxima in the PDFs, within a window of $x \pm 0.1$, are identified and if those

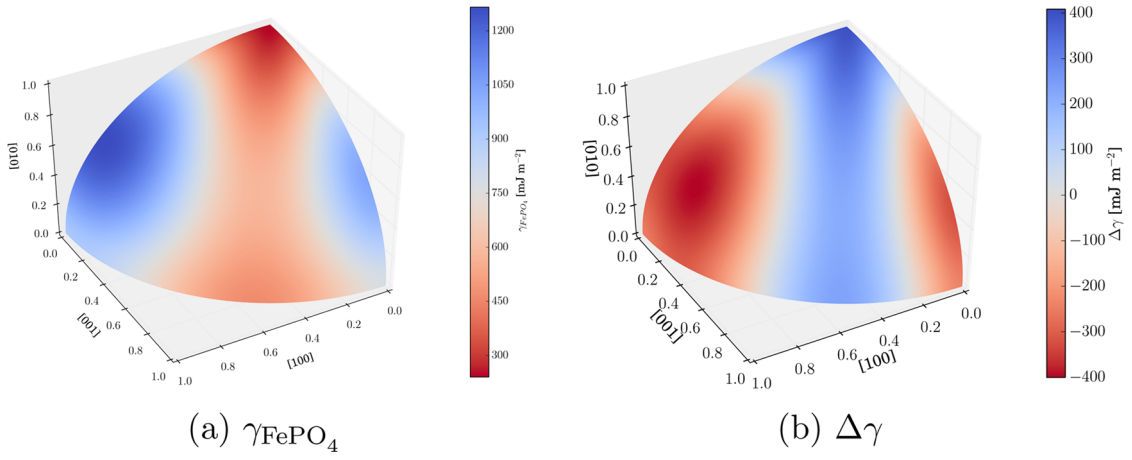

Figure 1. Interpolated surface energy of $FePO_4$ and difference in surface energy as a function of surface normal expressed in spherical coordinates using [010] as the pole. The color map is reversed such that the colors of panels b match with simulation results below.

maxima exceed $\sigma\sqrt{2\pi}\cdot\mathrm{PDF} > 0.05$, then that peak is inserted into the phase diagram. The resulting phase diagram therefore depends to some degree on the chosen variance, window and threshold but the usefuleness for this systematic procedure is demonstrated below.

Without Surface Wetting. To ensure that the simulated particles could evolve to a fully segregated concentration profile without encountering a nucleation barrier, a segregated profile was used as an initial condition. From the initially segregated profile, particles were free to evolve to homogeneity. For small particles that remained segregated, the total free energy was compared against auxiliary calculations of homogeneous particles at the same average concentration, which would not decompose spontaneously if they were outside the spinodal, which allowed us to ascertain with some confidence that we had obtained the equilibrium state.

The size-dependent phase diagram for spherical particles without wetting is shown in Figure 2 along the PDFs for 5, 10, and 40 nm particles in Figure 3. In Figure 2, particles of average concentration $\bar{x}$, denoted by symbols, segregate into volumes of average concentrations approximately x^{α} and x^{β}. Segregation is not always complete as indicated by the associated PDFs in Figure 3. As the particle radius decreases, segregation ceases to be energetically favorable, leading to the vanishing of the size-dependent solubility gap. The dashed gray line is intended to be a guide for the eye and is not representative of any data fitting.

In examining the PDFs at 5 nm, we see that the majority of particles are homogeneous with their distribution centered at their average concentration, indicating these particles evolved to be homogeneous from their segregated initial condition. Intermediate concentrations, however, $\bar{x}$ = 0.4, 0.5, and 0.6 have become smeared out over a range of local concentrations indicating a tendency to separate. As the particle

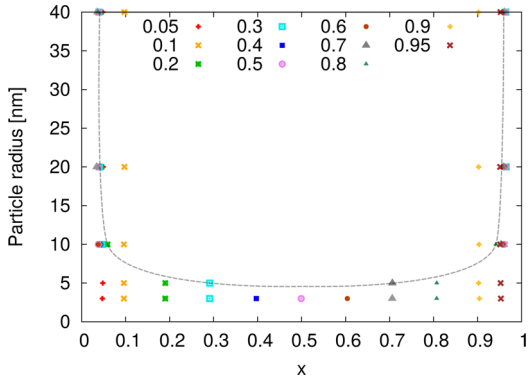

Figure 2. Simulated size-dependent phase diagram without considering surface wetting. Data points are grouped according to $\bar{x}$ and indicate peaks in the PDFs, corresponding to significant volumes of the particle at the corresponding local composition. The dashed gray line is a guide for the eye to show the approximate shape of the phase diagram and is not fit to data.

size increases, the tendency to phase-separate increases, but does not always result in peaks high enough to appear on the phase-diagram as per the above methodology. For 10 nm particles, for example, although peaks appear approximately at the expected solubility limits, too much material is still at intermediate concentrations indicating that the separation process is incomplete. It is interesting to note that the center of the peaks are also shifting with average particle concentrations. At 40 nm, the relative amount of material at intermediate concentrations has been reduced and the peaks have enlarged and are roughly centered around the same extrema: the solubility limits specified by the free energy diagram. Interestingly, $\bar{x}$ = 0.05, 0.1, 0.9, and 0.95 never separate: the initial conditions of complete segregation into the bulk equilibrium solubility limits always evolves to homogeneity.

The size-dependent cell voltage diagram is shown in Figure 4 arranged to show sections of constant average concentration and constant size. In Figure 4a,

lines connect data for the same $\bar{x}$ but for different particle sizes. As the particle size increases, the curves converge indicating two-phase coexistence. The unchanging homogeneity for $\bar{x}$ = 0.05, 0.1, 0.9, and 0.95 appear as vertical lines. In Figure 4b, lines connect data of particles of a particular size, with different $\bar{x}$. Figure 4b also includes the voltage diagram for the bulk material in which interfacial and surface energy may be neglected, so the only contribution to the free energy in eq 1 is the chemical free energy density *f*. To compare the effect of sample size, both the bulk two-phase and homogeneous voltage diagrams are shown. In this figure, the homogeneity of slightly (de)lithiated particles appear as extrema in *V* for (dis)charging. Particles of radius 3 and 5 nm are predicted to have a higher barrier height at concentrations 0.2 and 0.8. At 40 nm, the voltage varies between −4.96 and 4.85 mV from $Li_{0.2}FePO_4$ to $Li_{0.8}FePO_4$.

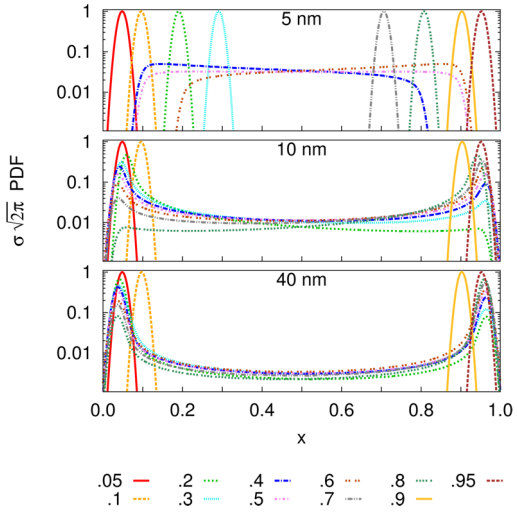

Figure 3. Probability density functions corresponding to particle radii 5, 10, and 40 nm. The 5 nm radius particle shows incomplete separation for $\bar{x}$ = 0.4, 0.5, and 0.6 and partial separation for the same concentrations for particle radius 10 nm. Particles with $\bar{x}$ = 0.05, 0.1, 0.9, and 0.95 are predicted not to separate for the investigated particle size range.

The simulation result of a 10 nm $Li_{0.8}FePO_4$ particle is shown in Figure 5 with contours denoting *x* = 0.3, 0.5, 0.7 and shows a convex surface. Averaging the normals of the undeformed *x* = 0.5, contour gives [0.857, 0.002, −0.515] which corresponds to a Miller surface of approximately (30 0 $\overline{37}$). The particle is also deformed quite strongly parallel to [100] which is easier to see on the projected (010) midplane on the bottom.

The simulation result of 40 nm $Li_{0.5}FePO_4$ is shown in Figure 6, showing a slightly warped plane. The deformation of this particle is barely visible due to its larger size, and the warping of the interface cannot be attributed to deformation. The average normal in the undeformed Cartesian coordinates is [0.855, 0.006, −0.519], which corresponds to a Miller surface of approximately (10 0 $\overline{11}$). A possible cause of the warping is illustrated in Figure 7 which shows the strain energy density inside the particle and looking along [010] direction, showing the increase in strain energy density bordering the surface.

With Surface Wetting. Possible microstructures for particles with surface wetting are not necessarily obvious. However, since surface wetting will drive segregation without a barrier to overcome, the nucleation of separate phases will not be an issue, although transformation between microstructures may not occur spontaneously. The initial condition plays a dominant role in determining to which microstructure the system will evolve; however, it is computational prohibitive to perform the large range of simulations required to be reasonably sure to have found the true lowest energy structure. The procedure we followed was to start with a randomly fluctuating *x* for 3 nm particles as the initial condition and propagate the steady state solution to increasing sizes. As the particles got larger, alternate microstructures sometimes evolved. Simulation results at 40 nm were then compared to another set of calculations at 40 nm with a fluctuation field as the initial condition. The lowest of the energies was then taken and propagated back down in size until the original

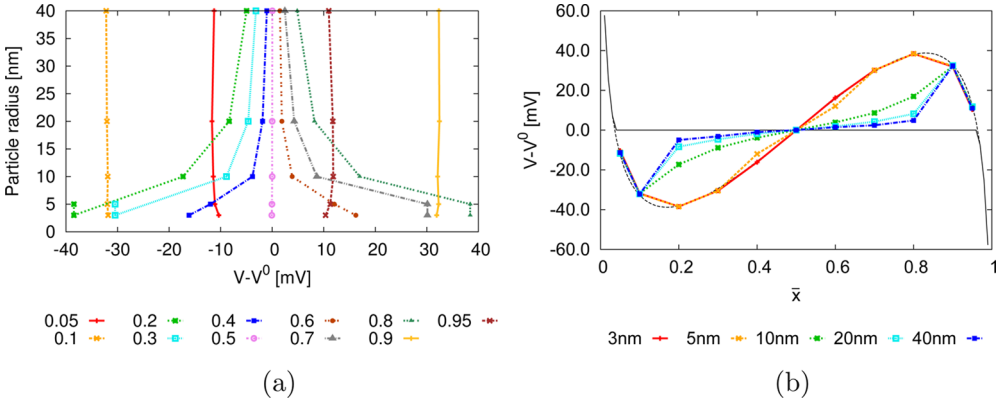

Figure 4. Two perspectives of the size-dependent map of voltage without surface wetting. In (a), each curve corresponds to a fixed concentration $\bar{x}$ with particle radius plotted against $V - V^0$; in (b), each curve corresponds to a fixed particle radius with $V - V^0$ plotted as a function of concentration $\bar{x}$. The black solid and dashed curves in (b) show the bulk two-phase and homogeneous voltage diagrams, respectively.

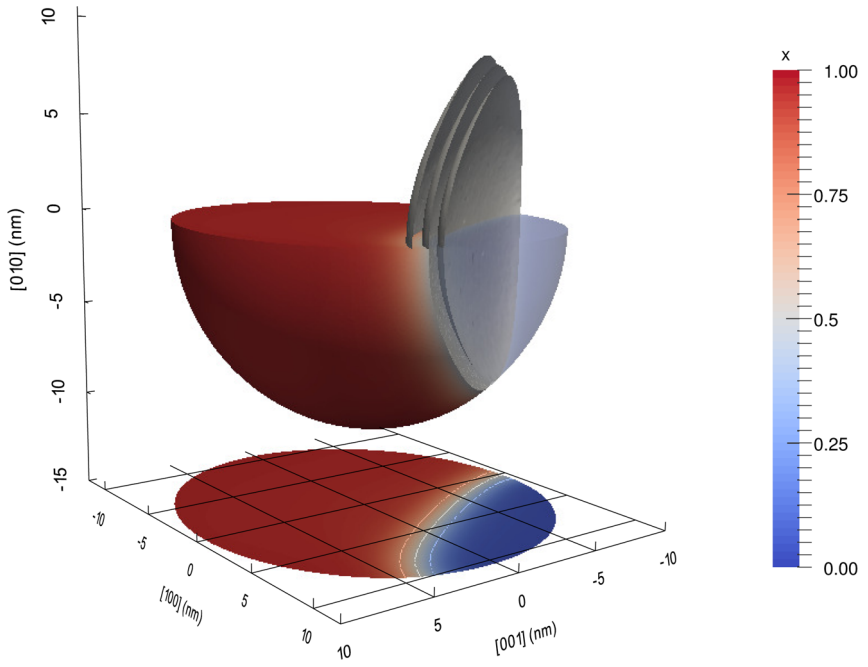

Figure 5. Simulation result for a 10 nm $Li_{0.8}FePO_4$ particle showing the $x = 0.3$, 0.5, and 0.7 contours. The 3D simulation results show the interface to be a convex dish shape, roughly aligned with [101]. The projected image on the bottom is the (010) surface which includes the origin, and shows that the interface is roughly aligned with [101]. Also visible is the deformation of the particle elongated along [100].

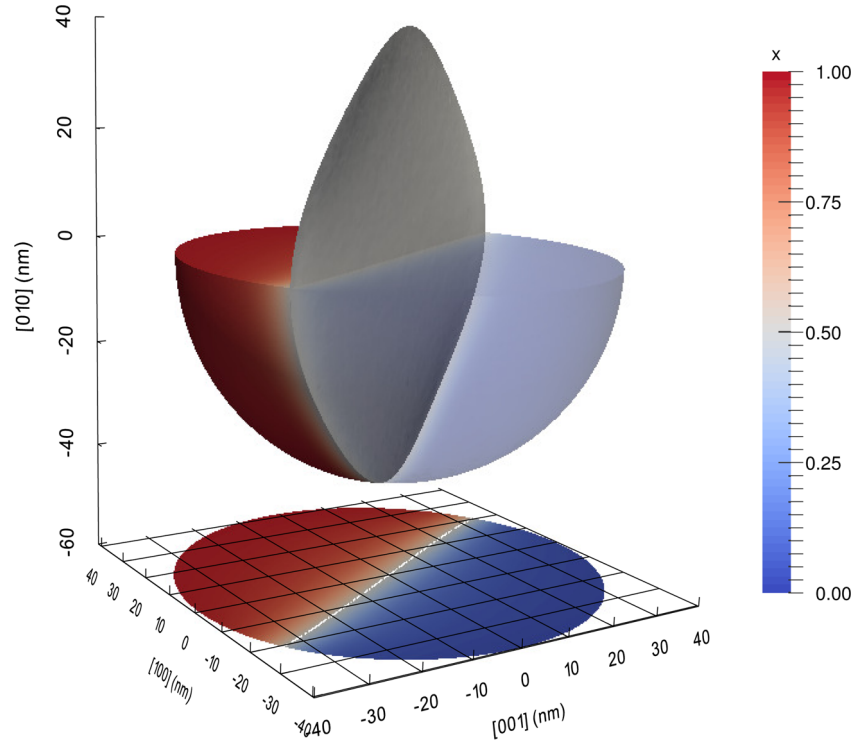

Figure 6. Simulation result for an $Li_{0.5}FePO_4$ particle showing the $x = 0.5$ contour as being warped but approximately $(\bar{1}0\ 0\ 11)$. The mid-(010) plane is projected onto the bottom of the figure and the contour denoted in white for visualization.

microstructure was found again. Therefore, two simulation results were sometimes available for some concentration/size pairs in which case the microstructure with the lowest integrated free energy is discussed here, unless otherwise noted.

The results the simulations including surface wetting for radii 5, 10, 20, and 40 nm with $\bar{x} = 0.1$ to 0.9 are shown in Figure 8. In considering this figure, the effect of the surface wetting force is clear, as the microstructure attempts to follow the facet-dependent difference

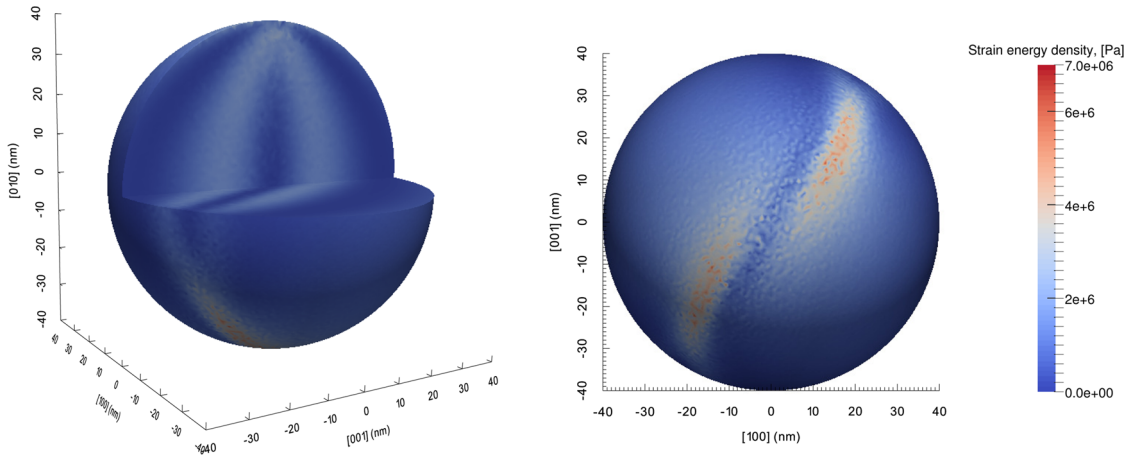

Figure 7. Simulated strain energy density for a 40 nm $Li_{0.5}FePO_4$ particle showing the structure of the stress around the interface pictured in Figure 6.

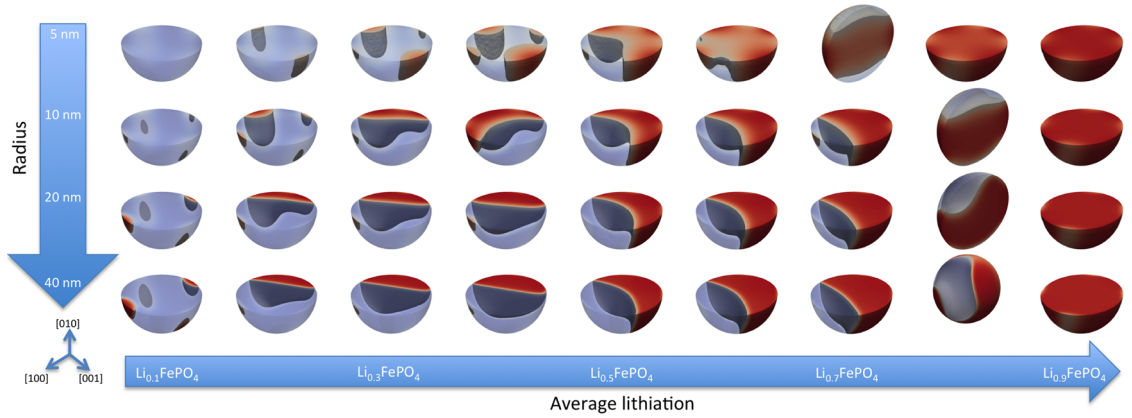

Figure 8. Summary of simulation results including surface wetting showing microstructural evolution as a function of particle radius and average concentration. Only results with the lowest free energy are shown. Surface wetting causes (de)lithiation of certain areas of the surface according to Figure 1b and competes with interfacial area minimization and anisotropic elasticity for dominance in determining the form and symmetry of the microstructure. Symmetries change for higher $\bar{x}$ and are absent for the 40 nm $Li_{0.8}FePO_4$ particle.

in surface energy shown in Figure 1b with varying degrees of success. The relative width of the interface and progression toward homogeneity can be seen by the surface colors for 5 nm particles, in particular $Li_{0.5}FePO_4$.

The size-dependent phase diagram of Li_xFePO_4 including the effects of surface wetting are shown in Figure 9 along with PDFs for 3, 5, 10, 20, and 40 nm particles in Figure 10. The situation is obviously more complex as indicated by the PDFs, which are much more spread out between solubility limits for smaller particles. As is expected from Figure 8, even small particles still show a range of lithiation. At larger sizes, separation becomes more complete as would be expected as bulk effects dominate those on the surface. Of particular note in the PDFs is the absence of any completely homogeneous particles as are found in Figure 3, although all small particles show a degree of the criteria of "homogeneity" in the sense of being spread out. The phase diagram on the surface of the sphere is qualitatively similar to Figure 9, as shown in the Supporting Information in Figure S2 with its associated PDFs in Figure S3.

The size-dependent voltage diagrams are shown in Figure 11. As before, the bulk two-phase and homogeneous voltage diagrams are included. The barriers in Figure 11b are absent for smaller particles and only begin to appear for particles larger than 40 nm radius. The constant concentration lines in Figure 11a show some sudden jumps, notably for $\bar{x}$ = 0.05, 0.1, 0.9, and 0.95 and also between 3 and 5 nm radii, which may be attributed to jumps between different microstructures. As before, the voltage at intermediate concentrations is not constant but varies from −4.21 to 6.8 mV from 40 nm $Li_{0.2}FePO_4$ to $Li_{0.8}FePO_4$. Figure 11b shows that the extrema on either side of $V = V^0$ are asymmetric, and seem to be shifting away from each other.

Particles with radius 40 nm perhaps show an interface similar to that of Figure 6. The normals of the interfaces of $Li_{0.3}FePO_4$ and $Li_{0.4}FePO_4$ were calculated as [0.789 −0.002 −0.615] and [0.796 −0.001 0.605], respectively, which both correspond approximately to

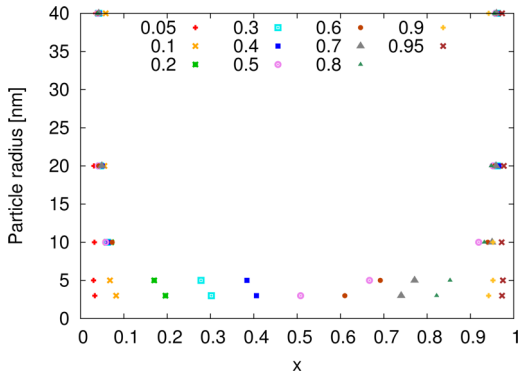

Figure 9. Size-dependent phase diagram including surface wetting. Data are grouped accord to $\bar{x}$ and show peaks in the PDFs. Particles below approximately 5 nm radius have a large volume fraction at the overall $\bar{x}$, but the peak shifts due to spreading out by surface wetting and interfacial effects.

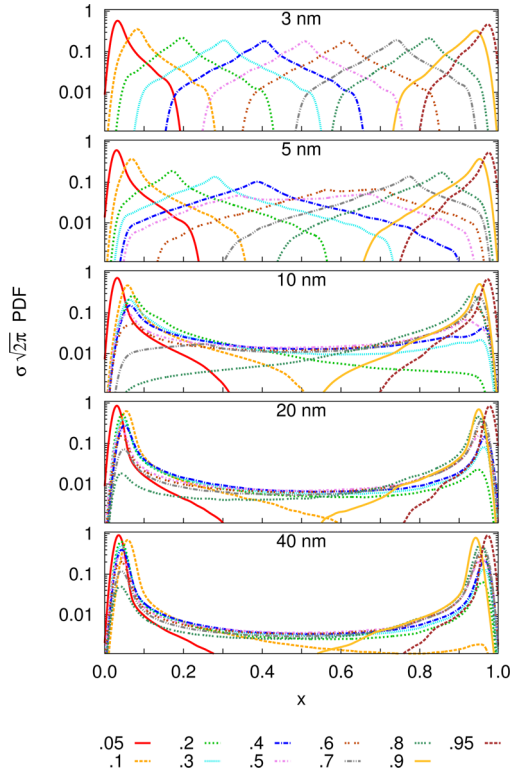

Figure 10. Probability density functions for simulations with surface wetting corresponding to particle radii 3, 5, 10, 20, and 40 nm. Particles generally show the full range of *x*, and while they tend to peak at the corresponding $\bar{x}$, the peaks are broad. No completely homogeneous particles are predicted.

Miller surfaces (25 0 40). Of note is that the [010] component is approximately zero, which supports the validity of the symmetry in that direction.

The alternative microstructure of $Li_{0.7}FePO_4$ is shown in Figure 12 and is interesting because of the changing symmetry of the results. Ascending in size, the steady state changes from mirror symmetry in all three lattice direction at 10 nm, to symmetry in the [001] and [100] at 20 nm, and then asymmetric in [001]. Of the simulation results, only the 40 nm $Li_{0.8}FePO_4$ shows no symmetry.

The magnitude of the components of the free energy for the ground state of $Li_{0.7}FePO_4$ is shown in Figure 13 by area filled curves, and the free energy of the alternative microstructure shown in Figure 12 indicated with a black dashed line. It should be understood that these energies correspond to an equilibrium state and the magnitude of the energy is therefore the "unrelaxed" energy that remains in the particle in global equilibrium. Therefore, the relative contribution of the surface energy diminishes with increasing size due to both the geometric shrinking of the surface to volume ratio, and also the "success" of the surface energy in (de)lithiating the surfaces without interference from the interface, which is more predominant in smaller particles. The contribution of the chemical free energy also decreases with size as more material is able to occupy the minima in the free energy. The contribution of the surface stress is negligible in all cases.

DISCUSSION

The phase diagrams presented in Figures 2 and 9 agree with experimental results of the vanishing of the miscibility gap below approximately 10 nm radius particles and does not seem to be affected by surface wetting. A caveat to this is the stability of slightly (de)lithiated particles, $\bar{x}$ = 0.05, 0.1, 0.9, 0.95 without surface wetting. These average concentrations appear to be stable in their uniform homogeneity to particle sizes larger than those simulated unless surface wetting is considered. The lack of decomposition for slightly (de)lithiated particles is readily explained as the energy cost of interface creation is greater than the benefit of decomposition for small particle sizes. This is a well-known size dependent effect, but because of the computational expense of increased particle sizes, decomposition was never observed in the current work.

As the miscibility gap decreases, the limits in either phase appear to depend on $\bar{x}$, an effect which is stronger with surface wetting. This shift was observed experimentally on faceted particles by Wagemaker *et al.*, although the extent of their reported shift was more pronounced even compared to the surface wetting case modeled here, possibly due in part to the faceted particle geometries.[12] This shift has been simulated with phase-field models with and without coherency strain.[12,14,18] In the current work, this effect could be seen to result from the interface attempting to minimize its area by reducing the volume of the minority phase which can be accomplished by raising the solubility limits.

The effect of particle size and surface wetting on the voltage diagrams may be seen in Figures 4b and 11b. In Figure 4b, the progression from the homogeneous profile to that of two-phase coexistence is readily explained as the interfacial energy which suppresses phase separation decreases in relative effect as particles get larger. Considering Figure 11b, the case is

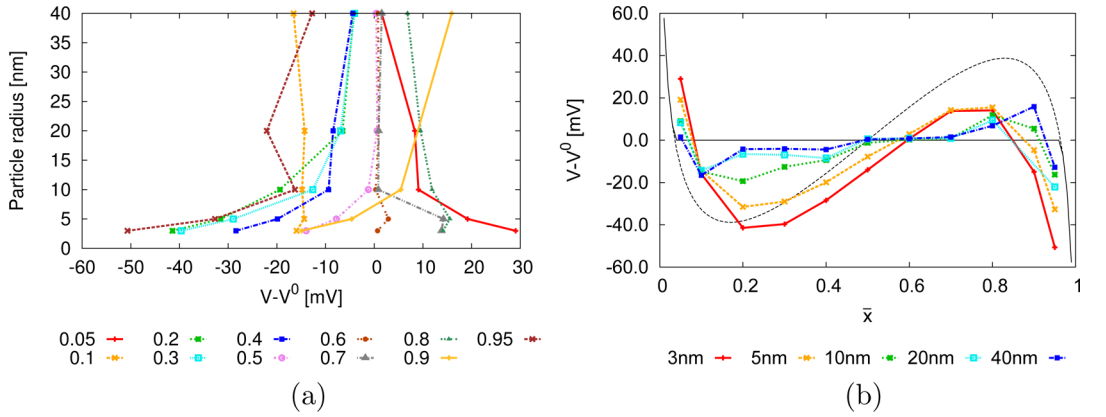

Figure 11. Two perspectives of the size-dependent map of voltage including surface wetting. In (a), each curve corresponds to a fixed concentration $\bar{x}$ with particle radius plotted against $V - V^0$; in (b), each curve corresponds to a fixed particle radius with $V - V^0$ plotted as a function of concentration $\bar{x}$. The nonsmooth behavior in (a) can be attributed to changes in microstructure, although these are not so apparent in (b). The black solid and dashed curves in (b) show the bulk two-phase and homogeneous voltage diagrams, respectively.

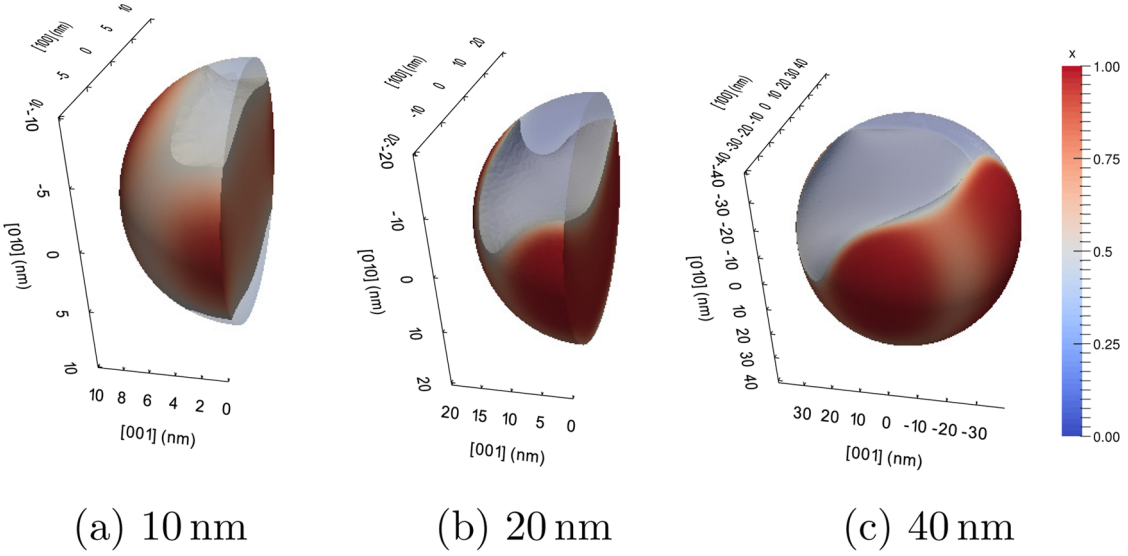

Figure 12. Metastable microstructures for $Li_{0.7}FePO_4$ particles for (a) 10 nm with symmetry in all three directions, (b) 20 nm with 2-fold symmetry, and (c) rotational symmetry for π rad around [010].

complicated as small, otherwise homogeneous particles are perturbed by surface wetting. As the particle size increases, the relative effect of surface wetting diminishes and the bulk behavior is approached.

The simulated voltage plateaus in Figures 4b and 11b are not flat at $V = V^0$ but slowly cross it at an angle in agreement with experiments.[28,41,42] This slope persists regardless of surface wetting, and decreases with increasing particle size. The change in the solubility limits described above, which implies changing minima in the global free energy curve, may also affect the equilibrium voltage that corresponds to the lowest common tangent of that curve. Alternately, this could be the result of a volumetric stress effect that scales linearly with average concentration. The fact that we predict this slope for a single particle is not in contradiction of Ferguson *et al.*,[42] who explain the experimental results as a consequence of a size distribution of particles. Rather, the experimentally observed slope would be the consequence of *both* single particle effects *and* size distribution.

The interface orientation without surface wetting is approximately $\{101\}$ with the 3D, concentration dependent constants as shown in Figure 6, and agrees with the experimental observations of Ramana *et al.*, and the constant moduli approximate analysis of Cogswell and Bazant.[14,15] The interface also appears slightly warped, which is an unexpected result. The particle is 40 nm in radius, which is above the range of influence of surface effects as indicated by Figure 10. Therefore, it is likely that elastic effects are the cause of this warping, possibly in a complicated fashion due to the combination of anisotropic interface mismatch and concentration dependent elastic moduli.

For $\bar{x} \neq 0.5$, the morphology is also affected by interface area minimization which favors inward facing

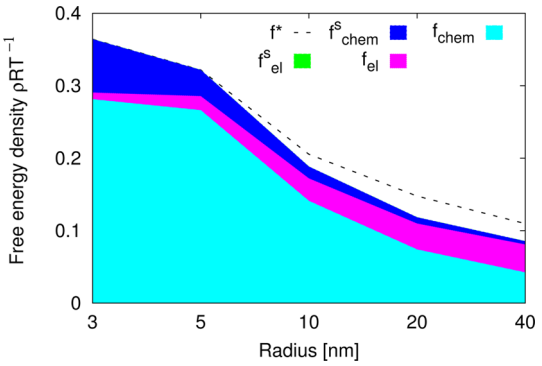

Figure 13. Plot of integrated volume and surface chemical free energy, f_{chem} and elastic energy, f_{el}, for $Li_{0.7}FePO_4$, divided by the particle volume. Filled areas are the energy components for the lowest energy state as shown in Figure 8, while the black dashed line labeled f^* shows the total free energy of the metastable microstructures shown in Figure 12.

concave interfaces. The {100} surfaces were never observed, possibly due to our simulating spherical particles whereas that interface orientation is more commonly observed on plate-like particles, although Ramana *et al.* also found them on their particles.[15,17] Alternately, using a semicoherent interface model may produce {100} surfaces, as predicted by Cogswell *et al.*[14]

When surface wetting is considered, the simulation results in Figure 8 show minority phases aligning themselves with a localized area of beneficial surface energy, overcoming the barrier to their formation in small particles. The overall interface morphology and orientation is governed more by connecting regions of strong surface wetting than elastic and structural effects. At small particle sizes, surface wetting is relatively stronger and the microstructure is determined by the balance between the surface forces, which attempt to reach Figure 1b, and confinement of the interface. To the extent of the authors' knowledge, such microstructures have not been observed experimentally for sphere-like particles.

Abrupt changes in microstructure show up as jumps in the voltage visible in Figure 11a, but not so obviously in Figure 11b. Realistic particles are unlikely to be ideally spherical which would reduce the number of stable microstructures due to less symmetries in the overall particle. Therefore, jumps in the potential would probably not be observed in experiments because of the reduced number of possible microstructures, as well as blurring of any such discrepancies when measurements are taken of collections of particles.

As the particle size increases, surface wetting becomes relatively weaker and it becomes unfavorable to have multiple interfaces. However, wetting can still determine the orientation of the interface despite the elastic optimum relevant to the nonwetting case. The results here are limited by computational expense; however, it is logical to assume that at large enough particle sizes, elastic effects will dominate over surface wetting entirely and the wetting and nonwetting cases would coincide. The preferred microstructure may also be influenced by the geometry of real particles, which will probably not be the ideal sphere approximated here. Geometry-dependent structural effects may then stabilize, for example, the alternative microstructure shown in Figure 12 as its energy is already fairly close to that of the predicted structure as shown in Figure 13.

The voltammograms as functions of average concentration are clearly affected by particle size and surface wetting as shown in Figures 4b and 11b. The extrema in the voltammograms shift outward with increasing size and reduce in magnitude. This is explainable by the reducing relative influence of the interfacial energy with increasing particle size. With surface wetting, the relative ease of forming small phase regions is reflected in Figure 11b where the extrema around, *i.e.*, $\bar{x} = 0.8$, occurs at a lower magnitude of $V - V_0$ compared to Figure 4b. This is due to the location of the minority $FePO_4$ phase around the [010] facet as seen in Figure 8. Similarly, the surface wetting of Li on the other sides as per Table S2 reduces the magnitude of the voltammogram extrema for low lithiation.

The reduction of the magnitude of the extrema in the voltammograms with increasing particle size is in contrast with the conclusions of Cogswell and Bazant who show the nucleation barrier increases with particle size.[32] This difference may be attributed to the particle size and geometry examined in the current work. As particles increase in size, elasticity dominates interfacial and surface effects, leading to the nucleation mechanism considered by Cogswell and Bazant. While the current work tends to a similar direction, larger particle sizes are prohibitively computationally expensive and outside the emphasis of the current work on phase microstructure. In addition, consideration of spherical particles here as compared to the plate-like particles inherently assumed in the depth-averaged approach may also affect this prediction by changing the influence of the (010) surface.

Stabilization of the minority phase also interferes with the complete phase segregation, and therefore, the modifications to the voltammograms are not trivial. This *smearing* of the concentration is highlighted in the PDFs in Figure 10. We also note that the length of the voltage plateau differs, and the range of voltages encountered increases. Julien *et al.* report modification of voltammograms in galvanostatic charge/discharge experiments on 20 nm radius particles before and after carbon coating.[28] Such a coating is known to affect the structure of the surface layer and so may significantly alter the surface energies of the phases and therefore the surface wetting effect.

All simulated microstructures, with the exception of large, slightly delithiated particles, show one plane of symmetry, likely due to the crystal symmetry expressed

through the elastic moduli and facet dependent surface wetting. The metastable 40 nm $Li_{0.7}FePO_4$ particle in Figure 12 shows an antisymmetric configuration, and the 40 nm $Li_{0.8}FePO_4$ shown in and Figure 8 is completely asymmetric. In both cases, the interface minimization effect has reduced the number of separate phases and the remaining Li-poor phase has relocated close toward the (010) facet due to the surface wetting minimum, and appears to spread out into the favorable troughs as per Figure 1b.

Some general conclusions regarding the appropriateness of certain approximations may be drawn from this work. The surface strain energy in eq 2 can be seen to be negligibly small in comparison to the surface chemical free energy by Figure 13. Similarly, the contribution of coherency stress to the interfacial energy is small but not completely negligible. It will slightly increase the energy of material in the diffuse interface and, in the Cahn−Hilliard model, broaden it beyond the intended width that was used to select κ. However, an extended, completely coherent interface is also not realistic, as defects will form in order to reduce the strain, a factor which is not considered in the current model. While surface wetting constitutes a significant influence on the surface concentration, Figure 8 shows that the concentration at the boundaries cannot be fixed according to the most energetically favorable phase.

While symmetries do appear with and without surface wetting for spherical particles, 3D modeling appears necessary since the orientation of these symmetries change with $\bar{x}$ and size. In addition, some average particle concentrations, such as 40 nm $Li_{0.8}FePO_4$, show no symmetry whatsoever. The same is likely true of other 3D geometries such as thin, platelike particles, although no direct conclusions on these can be reached based on the current work. The phase diagrams present a condensed view of phase separation but, in light of the PDFs discussed here, somewhat oversimplifies the results for small particles since it does not provide information about the smearing of concentrations.

Finally, concentration and facet dependent surface energy is clearly a strong influence on the behavior of these simulated nanoparticles, and refinement of these data would help elucidate the complex observed behavior. Notably, inclusion of the electrolyte in first principle calculations would be beneficial, as would a more realistic model of facet dependence than that included in this model.

CONCLUSION

In this work, we have developed a 3D model for decomposition of nanoscale Li_xFePO_4 including concentration dependent elastic moduli, misfit strain, anisotropic surface energy, and spinodal decomposition. The disappearance of the miscibility gap and shifting of the solubility lines with average concentration is predicted in agreement with experimental observations although not to the same extent.[12] These effects are a consequence of the relative size of the interface and its morphology as determined by its excess chemical and structural energy. In considering 3D linear elasticity with concentration dependent lattice and elastic constants, a surface approximately equivalent to $\{101\}$ appears to be the optimal orientation, as observed in HRTEM.[15] A slope in the voltage plateau during two phase coexistence is predicted in single particles and diminishes with increasing particle size.

Facet dependent surface wetting produces complex phase microstructures within the nanoparticles, which have not yet been observed experimentally. Spatially varying areas of surface wetting can stabilize small phase volumes by lowering their total energy. Voltammograms are modified accordingly, which may help explain the modification of voltammograms by carbon surface coatings.[28] Surface wetting may be affected by particle coatings, electrolyte, or other particle shapes which would expose other facets. This effect may then constitute an opportunity to engineer better battery performance by enhancing phase segregation to modify voltammograms or suppressing it to improve mechanical stability.

METHODS

Model Parameters. In this work, brackets and parentheses denote distributive multiplication and function arguments, respectively, vectors are denoted by an arrow over the symbol and bold symbols denote tensor quantities. A colon denotes a tensor contraction, $\boldsymbol{\sigma} : \epsilon_{el} \equiv \sum_{ij} \boldsymbol{\sigma}_{ij}\epsilon_{el,ij}$, and the projection of the strain onto the surface, written as $\boldsymbol{P} = \mathbf{1} - \hat{n}\otimes\hat{n}$, is equivalent to the tensor operation $\epsilon^{s}_{el,ij} = \sum_{kl} \boldsymbol{P}_{ik}\epsilon_{el,kl} : \boldsymbol{P}^{T}_{lj}$.

The local Helmholtz energy density follows a regular solution model,

$$f = 2RT[x\ln(x) + [1-x]\ln(1-x)] + \Omega x[1-x] \qquad (11)$$

where R is the ideal gas constant and $T = 298.15$ K is the temperature which is considered constant at room temperature. Zhou *et al.* showed that the electronic entropy that accompanies Li occupation is also important, and therefore, the mixing entropy should be doubled.[43,44] The equilibrium bulk solubility limits of 0.03 and 0.97 are fixed by choosing $\Omega = 183$ meV such that the local chemical free energy density is minimized by a mechanical mixture of phases at these compositions in accordance with the lowest common tangent.[6,7,11,32] The value of κ is determined by the interface width, 4 nm as previously discussed, and is taken in this work as $\rho^{-1}\kappa = 0.684\ \text{eV}\cdot\text{nm}^2$.[11] The energy barrier Ω is approximately 50% larger than that used by Cogswell *et al.*[14] and Tang *et al.*,[45] who included coherency strain in their fitting of these parameters.

The surface energy at an arbitrary orientation is obtained by expressing the data of Wang *et al.*[31] in spherical coordinates, which is summarized in the Supporting Information. We assume separability of the θ and ϕ components such that $\gamma_{FePO_4} = \Theta_{FePO_4}(\theta)\Phi_{FePO_4}(\phi) + 240$, and note that lattice symmetry

implies:

$$\frac{\partial \Phi_{FePO_4}}{\partial \phi}\left(\phi = \left\{0, \frac{\pi}{2}\right\}\right) = 0 \quad (12a)$$

$$\frac{\partial \Theta_{FePO_4}}{\partial \theta}\left(\theta = \left\{0, \frac{\pi}{2}\right\}\right) = 0 \quad (12b)$$

The polynomial fit is obtained with

$$\Phi_{FePO_4} = -1175\phi^5 + 3785\phi^4 - 3119\phi^3 + 52\phi^2 + 680 \quad (13a)$$

$$\Theta_{FePO_4} = 239\left[\frac{\theta}{\pi}\right]^4 - 255\left[\frac{\theta}{\pi}\right]^3 + 72\left[\frac{\theta}{\pi}\right]^2 \quad (13b)$$

Similarly, the interpolated function $\Delta\gamma$ is

$$\Delta\gamma = \Theta_{\Delta\gamma}(\theta)\Phi_{\Delta\gamma}(\phi) + 400 \quad (14)$$

with

$$\Phi_{\Delta\gamma} = -3030\phi^5 + 10591\phi^4 - 9792\phi^3 + 2724\phi^2 - 660 \quad (15a)$$

$$\Theta_{\Delta\gamma} = 124\left[\frac{\theta}{\pi}\right]^4 - 140\left[\frac{\theta}{\pi}\right]^3 + 43\left[\frac{\theta}{\pi}\right]^2 \quad (15b)$$

In the simulations, facet normals of exterior facets are scaled using the $FePO_4$ lattice constants from Maxisch *et al.*[20] summarized in Table S1 to get the corresponding Miller vector, and then interpolated using eq 14.

From the mass flux expression in eq 6, since $0 < x < 1$ and $\boldsymbol{D} \neq 0$, the chemical potential gradient must be equal to zero, corresponding to global thermodynamic equilibrium. The effect of $\boldsymbol{D}$ is as a kinetic parameter which will favor certain directions, but will not affect the finally state which is determined thermodynamically. To simplify the current work, we therefore take $\boldsymbol{D} = \mathbf{1}$ nm^2 s^{-1}.

We have not found any first-principle calculations of the surface elastic constants of $FePO_4$. However, typical surface elastic constants are of the order of 1 eV nm^{-2}.[36,46−48] As a working simple model we have therefore assumed an isotropic surface elastic stiffness of 1 eV nm^{-2}, such that $\boldsymbol{C}^s = 1_4$ eV·nm^2 where $\mathbf{1}_4$ is the rank-4 identity tensor. Note that this implies that $C^s_{1122} = 0$ but this is not unphysical since C^s_{1111} and C^s_{1122} are independent, and there is no physical constraint on the surface elastic tensor as there is for the bulk elastic tensor. The precise value of the elastic modulus is not particularly important in our case because other surface energy terms and the bulk elastic free energy dominate over surface elastic free energy even for particles of size ∼10 nm.

Assuring the Validity of the Computed *x*. During the course of the numerical computations, it was found that x was sometimes numerically calculated outside the range [0,1], which is an unphysical situation and numerically problematic because of the free energy definition, notably the logarithmic entropic terms in eq 11. To avoid this situation, a coordinate transformation on x, inspired by the equilibrium solution of the Allen−Cahn equation, is possible to define a new variable a such that

$$x = \frac{1}{2}\left[1 + \tanh(a)\right] \quad (16)$$

from which we note in particular $\partial x/\partial a = (1/2)\mathrm{sech}^2(a)$, $x[1 - x = (1/4)\mathrm{sech}^2(a)$, , and $\ln(x) - \ln(1 - x) = 2\ a$. With this transformation, eqs 5 become

$$\mu = \frac{1}{\rho}\left[4a - 2\tanh(a) - \frac{\kappa}{2}\nabla\cdot\mathrm{sech}^2(a)\nabla a + \frac{\partial \frac{1}{2}\boldsymbol{\sigma} : \epsilon_{el}}{\partial x}\right] \text{ on } V \quad (17)$$

$$0 = \frac{1}{\rho}\left[\Delta\gamma[1 + \mathrm{tr}(\epsilon^s)] + \hat{n}\cdot\frac{\kappa}{2}\mathrm{sech}^2(a)\nabla a\right] \text{ on } S$$

Finally, substituting into eq 6, the mass flux is rewritten as

$$\vec{J} = -\rho\ \mathrm{sech}^2(a)\frac{1}{RT}\boldsymbol{D}\cdot\nabla\mu \quad (18)$$

This transformation adds numerical complexity due to the need to compute hyperbolic secant but also eliminates the computation of the logarithms which arise from the derivative of eq 11. Since the transformation is inside the conserved flux definition, mass conservation is automatically enforced. Importantly, the assurance of the mole fraction's valid range allows the simulation of particles with average concentrations that approach the equilibrium concentrations to converge reliably.

Implementation. The coupled elasticity and diffusion model is described by the three coupled equations, eq 7 subject to eqs 8, 17, and 18 with the independent variables a, μ, and $\vec{u}$, respectively. Equations 17 and 18 are first written in the weak form using standard techniques, whereas the virtual energy formulation in eq 8 is already in a weak form. Numerical solutions are obtained using the Finite Element package FEniCS configured to use the PETSc library for scalable solution methods of partial differential equations.[49−56] Simulations are preformed on a high performance Linux computer cluster.

The system of nonlinear equations is solved using Newton's method with a GMRES Krylov iterative solver. The elastic and Cahn−Hilliard physics modes are strongly coupled through coherency strain at the interface. Therefore, the fully coupled system is solved directly as opposed to an operator-split method, which results in strong convergence at larger time steps at the cost of a moderate increase in computational expense. A physics based preconditioner using block Gauss-Seidel is used to split the elasticity from the Cahn−Hilliard, which was found experimentally to result in faster computations for larger system sizes. Both physics modes are solved using the Additive Schwarz method [ASM] preconditioner with overlap one, with either an LU or ILU(10) subsolver depending on the size of the subproblem. Computations are run on a number of cores ranging from 16 to 256 selected to keep the number of DOFs in the ASM subsolver roughly to 10 000, which we find balances time spent computing on each node with communicating between nodes.

To prevent arbitrary rigid body displacements and rotations, either the displacement may be "pinned" at certain vertices or the six 3D rigid body modes may be removed during the numerical solution process. We found experimentally that removing the rigid body modes at the solver level yielded order of magnitude reduction in Krylov iterations.

Each particle size requires a different mesh which was constructed *via* GMSH, with element sizes of 0.5 nm for particle radii 3, 5, and 10 nm, and 1 nm for particle radii 2, and 40 nm.[57] The increase in element width with particle size is possible by an increase in the size of simulated features, but is limited to adequate resolution of the interface, in this case at least four elements over the width of the interface.

Determining the equilibrium state requires finding the equilibrium, potentially complex interface morphology. A direct steady state calculation does not converge robustly, so a pseudotime approach is employed in which the time dependent equations above are run until steady state is reached. Steady state is defined as when the rate of change of the mole fraction is less than 10^{-6} s^{-1} everywhere in the simulation. The method was made efficient by using an adaptive time stepping method. The average Li fraction is calculated at each time step and varies by less than 10^{-10}, thus ensuring mass conservation.

Conflict of Interest: The authors declare no competing financial interest.

Acknowledgment. The authors would like to thank D. Wolf and P. Voorhees for many fruitful discussions and suggestions. We also gratefully acknowledge the computing resources provided on the Blues high-performance computing cluster operated by the Laboratory Computing Resource Center at Argonne National Laboratory. Part of the work at Argonne by M.J.W. and D.K. was funded by the Department of Energy, and partial support from the Department of Energy, Office of Science, Division of Materials Science and Engineering is gratefully acknowledged. O.H. and D.T.O. were funded by financial assistance award 70NANB14H012 from the U.S. Department of Commerce, National Institute of Standards and Technology as part of the Center for Hierarchical Material Design (CHiMaD).

Supporting Information Available: The Supporting Information is available free of charge on the ACS Publications website at DOI: 10.1021/acsnano.5b02555.

Summary of the elastic and structural constants, and surface energies in spherical coordinates (PDF)

REFERENCES AND NOTES

1. Li, D.; Zhou, H. Two-Phase Transition of Li-Intercalation Compounds in Li-Ion Batteries. *Mater. Today* **2014**, *17*, 451–463.
2. Wagemaker, M.; Mulder, F. M. Properties and Promises of Nanosized Insertion Materials for Li-Ion Batteries. *Acc. Chem. Res.* **2013**, *46*, 1206–15.
3. Van Der Ven, A.; Bhattacharya, J.; Belak, A. A. Understanding Li Diffusion in Li-Intercalation Compounds. *Acc. Chem. Res.* **2013**, *46*, 1216–1225.
4. Takahashi, M.; Shinichi, T.; Koji, T.; Yoji, S. Characterization of LiFePO4 as the Cathode Material for Rechargeable Lithium Batteries. *J. Power Sources* **2001**, *98*, 508–511.
5. Delmas, C.; Maccario, M.; Croguennec, L.; Le Cras, F.; Weill, F. Lithium Deintercalation in LiFePO4 Nanoparticles via a Domino-Cascade Model. *Nat. Mater.* **2008**, *7*, 665–671.
6. Yamada, A.; Koizumi, H.; Sonoyama, N.; Kanno, R. Phase Change in LixFePO4. *Electrochem. Solid-State Lett.* **2005**, *8*, A409.
7. Srinivasan, V.; Newman, J. Discharge Model for the Lithium Iron-Phosphate Electrode. *J. Electrochem. Soc.* **2004**, *151*, A1517.
8. Padhi, A.; Nanjundaswamy, K.; Goodenough, J. Phospho-olivines as Positive-Electrode Materials for Rechargeable Lithium Batteries. *J. Electrochem. Soc.* **1997**, *144*, 1188.
9. Meethong, N.; Huang, H.-Y. S.; Carter, W. C.; Chiang, Y.-M. Size-Dependent Lithium Miscibility Gap in Nanoscale Li[1-x]FePO4. *Electrochem. Solid-State Lett.* **2007**, *10*, A134.
10. Gibot, P.; Casas-Cabanas, M.; Laffont, L.; Levasseur, S.; Carlach, P.; Hamelet, S.; Tarascon, J.-M.; Masquelier, C. Room-Temperature Single-Phase Li Insertion/Extraction in Nanoscale LixFePO4. *Nat. Mater.* **2008**, *7*, 741–747.
11. Bai, P.; Cogswell, D. A.; Bazant, M. Z. Suppression of Phase Separation in LiFePO4 Nanoparticles During Battery Discharge. *Nano Lett.* **2011**, *11*, 4890–4896.
12. Wagemaker, M.; Singh, D. Dynamic Solubility Limits in Nanosized Olivine LiFePO4. *J. Am. Chem. Soc.* **2011**, *133*, 10222–10228.
13. Kobayashi, G.; Nishimura, S.-i. I.; Park, M.-S. S.; Kanno, R.; Yashima, M.; Ida, T.; Yamada, A. Isolation of Solid Solution Phases in Size-Controlled LixFePO4 at Room Temperature. *Adv. Funct. Mater.* **2009**, *19*, 395–403.
14. Cogswell, D. A.; Bazant, M. Z. Coherency Strain and the Kinetics of Phase Separation in LiFePO4 Nanoparticles. *ACS Nano* **2012**, *6*, 2215–2225.
15. Ramana, C.; Mauger, A.; Gendron, F.; Julien, C.; Zaghib, K. Study of the Li-Insertion/Extraction Process in LiFePO4/FePO4. *J. Power Sources* **2009**, *187*, 555–564.
16. Laffont, L.; Delacourt, C.; Gibot, P.; Wu, M. Y.; Kooyman, P.; Masquelier, C.; Tarascon, J. M. Study of the LiFePO4 / FePO4 Two-Phase System by High-Resolution Electron Energy Loss Spectroscopy. *Chem. Mater.* **2006**, *18*, 5520–5529.
17. Chen, G.; Song, X.; Richardson, T. J. Electron Microscopy Study of the LiFePO4 to FePO4 Phase Transition. *Electrochem. Solid-State Lett.* **2006**, *9*, A295.
18. Burch, D.; Bazant, M. Z. Size-Dependent Spinodal and Miscibility Gaps for Intercalation in Nanoparticles. *Nano Lett.* **2009**, *9*, 3795–3800.
19. Meethong, N.; Kao, Y.-H.; Tang, M.; Huang, H.-Y.; Carter, W. C.; Chiang, Y.-M. Electrochemically Induced Phase Transformation in Nanoscale Olivines Li[1-x]FePO4 (M = Fe, Mn). *Chem. Mater.* **2008**, *20*, 6189–6198.
20. Maxisch, T.; Ceder, G. Elastic Properties of Olivine LixFePO4 from First Principles. *Phys. Rev. B: Condens. Matter Mater. Phys.* **2006**, *73*, 174112.
21. Wagemaker, M.; Mulder, F. M.; van der Ven, A. The Role of Surface and Interface Energy on Phase Stability of Nanosized Insertion Compounds. *Adv. Mater.* **2009**, *21*, 2703–2709.
22. Tang, M.; Belak, J. F.; Dorr, M. R. Anisotropic Phase Boundary Morphology in Nanoscale Olivine Electrode Particles. *J. Phys. Chem. C* **2011**, *115*, 4922–4926.
23. Khachaturyan, A. G. *Theory of Structural Transformations in Solids*; Dover Books on Engineering Series; Dover Publications: Mineola, NY, 2008.
24. Chen, G.; Song, X.; Richardson, T. J. Metastable Solid-Solution Phases in the LiFePO4/ FePO4 System. *J. Electrochem. Soc.* **2007**, *154*, A627.
25. Boesenberg, U.; Meirer, F.; Liu, Y. Mesoscale Phase Distribution in Single Particles of LiFePO4 Following Lithium Deintercalation. *Chem. Mater.* **2013**, *25*, 1664–1672.
26. Gouveia, D. X.; Lemos, V.; De Paiva, J. A. C.; Souza Filho, A. G.; Mendes Filho, J.; Lala, S. M.; Montoro, L. A.; Rosolen, j. M. Spectroscopic Studies of LixFePO4 and LixM0.03-Fe0.97PO4 (M = Cr,Cu,Al,Ti). *Phys. Rev. B: Condens. Matter Mater. Phys.* **2005**, *72*, 024105.
27. Van Der Ven, A.; Wagemaker, M. Effect of Surface Energies and Nano-Particle Size Distribution on Open Circuit Voltage of Li-Electrodes. *Electrochem. Commun.* **2009**, *11*, 881–884.
28. Julien, C. M.; Mauger, A.; Zaghib, K. Surface Effects on Electrochemical Properties of Nano-Sized LiFePO4. *J. Mater. Chem.* **2011**, *21*, 9955.
29. Zaghib, K.; Mauger, A.; Gendron, F.; Julien, C. M. Relationship Between Local Structure and Electrochemical Performance of LiFePO4 in Li-Ion Batteries. *Ionics* **2008**, *14*, 271–278.
30. Lucas, I. T.; Mcleod, A. S.; Syzdek, J. S.; Middlemiss, D. S.; Grey, C. P.; Basov, D. N.; Kostecki, R. IR Near-Field Spectroscopy and Imaging of Single LixFePO4Microcrystals. *Nano Lett.* **2015**, *15*, 1.
31. Wang, L.; Zhou, F.; Meng, Y.; Ceder, G. First-Principles Study of Surface Properties of LiFePO4: Surface Energy, Structure, Wulff Shape, and Surface Redox Potential. *Phys. Rev. B: Condens. Matter Mater. Phys.* **2007**, *76*, 165435.
32. Cogswell, D. A.; Bazant, M. Z. Theory of Coherent Nucleation in Phase-Separating Nanoparticles. *Nano Lett.* **2013**, *13*, 3036–3041.
33. Singh, G. K.; Ceder, G.; Bazant, M. Z. Intercalation Dynamics in Rechargeable Battery Materials: General Theory and Phase-Transformation Waves in LiFePO4. *Electrochim. Acta* **2008**, *53*, 7599–7613.
34. Zeng, Y.; Bazant, M. Z. Phase Separation Dynamics in Isotropic Ion-Intercalation Particles. *SIAM J. Appl. Math.* **2014**, *74*, 980–1004.
35. Dargaville, S.; Farrell, T. W. The Persistence of Phase-Separation in LiFePO4 with Two-Dimensional Li+ Transport: The Cahn-Hilliard-Reaction Equation and the Role of Defects. *Electrochim. Acta* **2013**, *94*, 143–158.
36. Yvonnet, J.; Mitrushchenkov, A.; Chambaud, G.; He, Q. C. Finite Element Model of Ionic Nanowires with Size-Dependent Mechanical Properties Determined by Ab-initio Calculations. *Comput. Methods Appl. Mech. Eng.* **2011**, *200*, 614–625.
37. Gránásy, L.; Pusztai, T.; Saylor, D.; Warren, J. A. Phase Field Theory of Heterogeneous Crystal Nucleation. *Phys. Rev. Lett.* **2007**, *98*, 035703.
38. Bazant, M. Z. Theory of Chemical Kinetics and Charge Transfer Based on Nonequilibrium Thermodynamics. *Acc. Chem. Res.* **2013**, *46*, 1144–1160.
39. Cahn, J. W. Critical Point Wetting. *J. Chem. Phys.* **1977**, *66*, 3667.
40. Ichitsubo, T.; Tokuda, K.; Yagi, S.; Kawamori, M.; Kawaguchi, T.; Doi, T.; Oishi, M.; Matsubara, E. Elastically Constrained Phase-Separation Dynamics Competing with the Charge Process in the LiFePO4/FePO4 System. *J. Mater. Chem. A* **2013**, *1*, 2567–2577.
41. Dreyer, W.; Jamnik, J.; Guhlke, C.; Huth, R.; Moskon, J.; Gaberscek, M. The Thermodynamic Origin of Hysteresis in Insertion Batteries. *Nat. Mater.* **2010**, *9*, 448–453.
42. Ferguson, T. R.; Bazant, M. Z. Phase Transformation Dynamics in Porous Battery Electrodes. *Electrochim. Acta* **2014**, *146*, 89–97.
43. Zhou, F.; Maxisch, T.; Ceder, G. Configurational Electronic Entropy and the Phase Diagram of Mixed-Valence

Oxides: The Case of LixFePO4. *Phys. Rev. Lett.* **2006**, *97*, 155704.
44. Malik, R.; Zhou, F.; Ceder, G. Kinetics of Non-Equilibrium Lithium Incorporation in LiFePO4. *Nat. Mater.* **2011**, *10*, 587–590.
45. Tang, M.; Huang, H. Y.; Meethong, N.; Kao, Y. H.; Carter, W. C.; Chiang, Y. M. Model for the Particle Size, Overpotential, and Strain Dependence of Phase Transition Pathways in Storage Electrodes: Application to Nanoscale Olivines. *Chem. Mater.* **2009**, *21*, 1557–1571.
46. Izumi, S.; Hara, S.; Kumagai, T.; Sakai, S. A Method for Calculating Surface Stress and Surface Elastic Constants by Molecular Dynamics: Application to the Surface of Crystal and Amorphous Silicon. *Thin Solid Films* **2004**, *467*, 253–260.
47. Reuter, K.; Scheffler, M. Composition, Structure and Stability of RuO_2(110) as a Function of Oxygen Pressure. *Phys. Rev. B: Condens. Matter Mater. Phys.* **2001**, *65*, 035406.
48. Miller, R. E.; Shenoy, V. B. Size-Dependent Elastic Properties of Nanosized Structural Elements. *Nanotechnology* **2000**, *11*, 139–147.
49. Balay, S.; Abhyankar, S.; Adams, M. F.; Brown, J.; Brune, P.; Buschelman, K.; Eijkhout, V.; Gropp, W. D.; Kaushik, D.; Knepley, M. G. *PETSc Users Manual*; ANL-95/11 Rev 3.6; Argonne National Laboratory: Argonne, IL, **2014**
50. Balay, S.; Brown, J.; Buschelman, K.; Gropp, D. W.; Kaushik, D.; Knepley, M.; McInnes, L.; Smith, F. B.; H, Z. PETSc Web page, http://www.mcs.anl.gov/petsc (accessed May 2015).
51. Balay, S., Gropp, W. D., McInnes, L. C., Smith, B. F. In *Modern Software Tools for Scientific Computing*; Arge, E., Bruaset, A. M., Langtangen, H. P., Eds.; Birkhäuser: Boston, MA, 1997; pp 163−202.
52. Logg, A., Mardal, K.-A., Wells, G. N. . *Automated Solution of Differential Equations by the Finite Element Method*; Logg, A., Mardal, K.-A., Wells, G., Eds.; Lecture Notes in Computational Science and Engineering; Springer: Berlin, Heidelberg, 2012; Vol. 84.
53. Logg, A.; Wells, G. N.; Hake, J. In *Automated Solution of Differential Equations by the Finite Element Method*; Logg, A., Mardal, K.-A., Wells, G. N., Eds.; Lecture Notes in Computational Science and Engineering; Springer: New York, 2012; Vol. 84, Chapter 10.
54. Alnæs, M. S. In *Automated Solution of Differential Equations by the Finite Element Method*; Logg, A., Mardal, K.-A., Wells, G. N., Eds.; Lecture Notes in Computational Science and Engineering; Springer: New York, 2012; Vol. 84, Chapter 17.
55. Kirby, R. C.; Logg, A. A compiler for variational forms. *ACM Trans. Math. Softw.* **2006**, *32*, 417–444.
56. Kirby, R. C. In *Automated Solution of Differential Equations by the Finite Element Method*; Logg, A., Mardal, K.-A., Wells, G. N., Eds.; Lecture Notes in Computational Science and Engineering; Springer: New York, 2012; Vol. 84, Chapter 13.
57. Geuzaine, C.; Remacle, J.-F. Gmsh: a Three-Dimensional Finite Element Mesh Generator with Built-in Pre- and Post-Processing Facilities. *Int. J. Numer. Methods Eng.* **2009**, *79*, 1309–1331.